

TECHNICAL NOTE**Sinusoidal Sensitivity Calculation for Line Segment Geometries**Luciano Vinas¹ | Atchar Sudyadhom^{2,3}¹Department of Statistics, UCLA, Los Angeles, California, USA²Department of Radiation Oncology, Dana-Farber Cancer Institute | Brigham and Women's Hospital, Boston, Massachusetts, USA³Department of Medical Physics in Radiation Oncology, Harvard Medical School, Boston, Massachusetts, USA**Correspondence**

Luciano Vinas, Mathematical Sciences, UCLA, 520 Portola Plaza, Los Angeles, CA. Email: lucianovinas@g.ucla.edu

Funding Information

This work was partially supported by NIBIB of the National Institutes of Health; Award number: R21EB026086

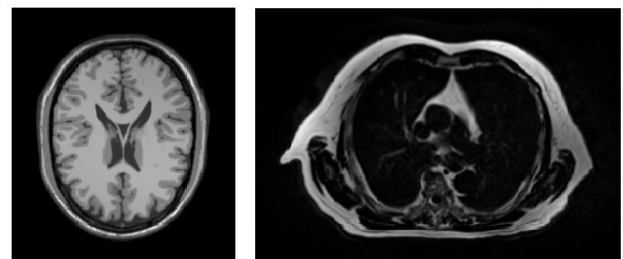
Purpose: Provide a closed-form solution to the sinusoidal coil sensitivity model proposed by Kern et al. This closed-form allows for precise computations of varied, simulated bias fields for ground-truth debias datasets.**Methods:** Fourier distribution theory and standard integration techniques were used to calculate the Fourier transform for line segment magnetic fields.**Results:** A $L^1_{loc}(\mathbb{R}^3)$ function is derived in full generality for arbitrary line segment geometries. Sampling criteria and equivalence to the original sinusoidal model are also discussed. Lastly a CUDA accelerated implementation `biasgen` is provided by authors.**Conclusion:** As the derived result is influenced by coil positioning and geometry, practitioners will have access to a more diverse ecosystem of simulated datasets which may be used to compare prospective debiasing methods.**KEYWORDS:**

sinusoidal sensitivity, coil sensitivity maps, bias fields, distribution theory, sparse sampling

1 | INTRODUCTION

The success of parallel imaging methods in magnetic resonance (MR) imaging have allowed for quicker image acquisition with little or no cost to spatial aliasing¹. Image reconstruction quality is dependent on how closely the gains of different radiofrequency (RF) coil contributions can be approximated. These gain normalization maps, also known as coil sensitivity maps or sensitivity maps for short, can be difficult to estimate at scan time. When incorrectly normalized, the different coil contributions can form a series of spatial inhomogeneities known bias fields in the final reconstructed image.

Fortunately, there is a rich literature of image post-processing techniques which aim to amend the MR bias field problem^{2,3}. These techniques may assume a smooth prior on the generated bias field or may choose a supervised approach to correcting bias fields⁴. Currently in the bias field literature, there is a limitation in the diversity of simulated datasets



(a) T1-weighted BrainWeb sample with simulated bias (b) T1-weighted thorax MR with scanner bias

FIGURE 1 Bias field comparison between 40% INU BrainWeb and patient thorax MR image. Relative to subfigure (a), subfigure (b) showcases sharp bias intensities at anatomy boundary.

which may be used for debias benchmarking. Furthermore these simulated datasets are generally limited in the bias fields they produce, opting instead for a single bias functional form with varied tissue contrasts and noise settings.

One example of this trend can be seen in the popular BrainWeb dataset of Ref. [5]. This dataset contains ground-truth MR intensities of a known head phantom while additionally providing a finite selection of multiplicative non-uniformity intensities (INU) and additive measurement noises which may be added on top of the ground-truth intensities. It should be noted the bias fields generated by this dataset can be fairly smooth, even when applied with the extreme INU setting. To add on, the INU parametrization of BrainWeb controls the overall scale of the bias intensity not its functional form. Figure 1 showcases an example of the difference in bias fields between a 40% INU BrainWeb slice and a real patient thorax MR image slice. Although the anatomy and coil cages are not equivalent in the example provided, Figure 1 still highlights the need to have varied, simulated bias fields when developing fully general debiasing algorithms.

In an ideal setting, our debias testing environment should contain a wide range of physically-viable bias fields with empirically supported functional forms. One prospective model is mentioned in Ref. [6] states that observed sensitivity maps may be approximated by sparse Fourier representations of the initial emitted magnetic field. This is a model which is already applied by other popular medical software such as the Berkeley Advanced Reconstruction Toolbox⁷ (BART). A current hang-up of the method is that computing the full required Fourier transform may be too computationally intensive or not numerically sensitive enough when using computational approximations such as the fast Fourier transform. Practical implementations of the model, like the one done by BART, use a small selection of dominant frequencies from an empirically verified source and then apply the fixed sensitivity maps to different phantoms and tissue contrasts.

The goal of this paper will be to provide a closed-form to sinusoidal sensitivity model of Ref. [6] for a restricted but expressive class of magnetic fields. In particular we are interested in the sensitivity maps produced by magnetic fields generated from segmented line geometries. The equation of focus will be

$$S(x) = \sum_{\omega \in G} e^{-i\omega \cdot x} \mathcal{F}\{\bar{B}(x)\}(\omega), \quad (1)$$

where $G \subset \mathbb{R}^3$ is a finite grid of points and

$$\bar{B}(x) = B(x) \cdot (u + iv) \quad (2)$$

is the measured magnetic field of source $B(x)$ according to some readout direction $u \in \mathbb{R}^3$ and phase encoding direction $v \in \mathbb{R}^3$. Notice as the sensitivity (1) and the measurement (2) are linear in emitted magnetic field B and the field B itself follows the superposition property, it will be sufficient for our purposes to calculate the Fourier transform for a single line segment magnetic field.

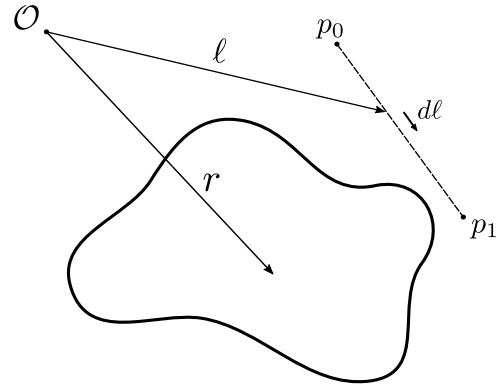


FIGURE 2 Line segment under consideration. Segment endpoints specified by p_0, p_1 with a magnetic field B evaluated at point r .

2 | LINE SEGMENT MAGNETIC FIELD

The contribution of an infinitesimal line segment $d\ell$ can be calculated using Biot-Savart law,

$$dB(x) = \frac{\mu_0 I}{4\pi} \frac{d\ell \times (x - \ell)}{\|x - \ell\|_2^3}.$$

Assuming a constant current I , the total magnetic field is proportional to

$$B(x) \propto \int_C \frac{\widehat{d\ell} \times (x - \ell)}{\|x - \ell\|_2^3},$$

for some line segment C . Any simple line segment C can be parameterized as

$$C(t) = p_0(1 - t) + tp_1, \quad \text{for } t \in [0, 1].$$

A change of variables reveals

$$\widehat{d\ell} = \frac{p_1 - p_0}{\|p_1 - p_0\|_2} dt.$$

With shorthands $a = p_1 - p_0$ and $b = x - p_0$ we have

$$B(x) \propto \frac{a \times b}{\|a\|_2} \int_0^1 \frac{dt}{\|b - at\|_2^3}.$$

This integral has the following solution

$$\left(\frac{a \times b}{\|a\|_2^2 \|b\|_2^2 - (a \cdot b)^2} \right) \frac{-a \cdot (b - at)}{\|a\|_2 \|b - at\|_2} \Big|_0^1.$$

With the additional shorthand $c = b - a$,

$$B(x) \propto \frac{(\hat{a} \times \hat{b})}{\|a\|_2 \|b\|_2 (1 - (\hat{a} \cdot \hat{b})^2)} (\hat{a} \cdot \hat{b} - \hat{a} \cdot \hat{c}).$$

Using identity $\|a \times b\|_2^2 = \|a\|_2^2 \|b\|_2^2 - (a \cdot b)^2$, we arrive at the final symmetric form

$$B(x) \propto \frac{(\hat{a} \cdot \hat{b})(\hat{a} \times \hat{b})}{\|a\|_2 \|b\|_2 (1 - (\hat{a} \cdot \hat{b})^2)} - \frac{(\hat{a} \cdot \hat{c})(\hat{a} \times \hat{c})}{\|a\|_2 \|c\|_2 (1 - (\hat{a} \cdot \hat{c})^2)}.$$

3 | FOURIER TRANSFORM OF A LINE MAGNETIC FIELD

Recall the measured magnetic field $\vec{B}(x) = B(x) \cdot (u + iv)$. Calculating (1) simplifies to calculating the Fourier transform for functions of the form

$$T^{(p_0)}(x) = \frac{(\hat{a} \cdot \hat{b})(u \cdot (\hat{a} \times \hat{b}))}{\|a\|_2 \|b\|_2 (1 - (\hat{a} \cdot \hat{b})^2)}.$$

When integrating we will consider the change of variable

$$x' = H^T(x - p_0)$$

where H is an orthonormal rotation matrix. We are interested in rotating to the orthogonal basis

$$B = \{\omega - \hat{a}(\omega \cdot \hat{a}), \omega \times a, a\},$$

with coordinate representations $a' = (0, 0, \|a\|_2)$ and $\omega' = (\omega'_x, 0, \omega'_z)$. In particular we align a' with the (+z)-axis and place ω' in the (+x, z)-halfspace. For this reason we will assume $\omega'_x > 0$ throughout without loss of generality. Additionally we note in the case ω and a are collinear, the Fourier transform $\mathcal{F}\{T\}(\omega) = 0$ regardless of choice of basis.

This change of variables produces the following simplifications

$$\begin{aligned} \|b\|_2 &= \|x'\|_2, \\ a \cdot b &= (H^T a) \cdot x', \\ u \cdot (a \times b) &= u \cdot (H H^T a) \times (H x') \\ &= (H^T u) \cdot (H^T a) \times x', \end{aligned}$$

where $H^T a = (0, 0, \|a\|_2)$.

As the choice of basis B is independent to input b , the x' transformation can be adapted to $T^{(p_1)}$ with $x'' = H^T(x - p_1)$. Next defining $T = T^{(p_0)} - T^{(p_1)}$ we can combine relevant integrations as so

$$\begin{aligned} \int T(x) e^{i\omega \cdot x} dx &= \int T^{(p_0)}(x) e^{i\omega \cdot x} dx - \int T^{(p_1)}(x) e^{i\omega \cdot x} dx \\ &= (e^{i\omega' \cdot H^T p_0} - e^{i\omega' \cdot H^T p_1}) \int T^{(0)}(x') e^{i\omega' \cdot x'} dx' \end{aligned}$$

For shorthand we introduce

$$\begin{aligned} A &= e^{i\omega' \cdot H^T p_0} - e^{i\omega' \cdot H^T p_1} \\ &= -i \sin(\|a\|_2 \omega'_z / 2) e^{i\omega' \cdot H^T (p_1 + p_0) / 2}, \end{aligned}$$

where equality follows from $\omega' \cdot H^T(p_1 - p_0) = \omega'_z \|a\|_2$.

Now we begin the task of calculating the Fourier transform of T . We will suppress all prime notation as it is understood that integration will be done in the rotated coordinates.

Integrating with spherical coordinates

$$\begin{aligned} \mathcal{F}\{T\}(\omega) &= \frac{A}{\|a\|_2} \int_0^\infty \int_0^\pi \int_0^{2\pi} \left(\frac{\cos \theta}{r(1 - \cos^2 \theta)} \right) \\ &\quad (\sin \theta (u_y \cos \phi - u_x \sin \phi) e^{ir(\omega_x \cos \phi \sin \theta + \omega_z \cos \theta)}) \\ &\quad (r^2 \sin \theta) d\phi d\theta dr \end{aligned}$$

Contribution $u_x \sin \phi$ can be dropped as

$$\int_0^{2\pi} u_x \sin \phi e^{ir\omega_x \cos \phi \sin \theta} = \frac{i}{r\omega_x \sin \theta} e^{ir\omega_x \cos \phi \cos \theta} \Big|_{\phi=0}^{2\pi} = 0.$$

Next expand $e^{i\eta} = \cos \eta + i \sin \eta$, symmetrize integration bounds, and simplify all odd (θ, ϕ) -function contributions

$$\begin{aligned} \mathcal{F}\{T\}(\omega) &= 2u_y \frac{A}{\|a\|_2} \int_0^\infty \int_{-\pi/2}^{\pi/2} \int_{-\pi/2}^{\pi/2} (r \sin \theta \sin \phi) \\ &\quad (\sin(r\omega_x \sin \phi \cos \theta) \sin(r\omega_z \sin \theta)) d\phi d\theta dr. \end{aligned}$$

Although we see now the integrand does not lie in $L^1(\mathbb{R}^3)$, the Fourier transform of T does still exist in a distributional sense. If T is a tempered distribution for the Schwartz class $\mathcal{S}(\mathbb{R}^3)$ then the Fourier transform of T can be defined by $\mathcal{F}\{T\}$ which satisfies

$$\int \mathcal{F}\{T\}(\omega) \varphi(\omega) d\omega = \int T(x) \mathcal{F}\{\varphi\}(x) dx \quad \forall \varphi \in \mathcal{S}(\mathbb{R}^3). \quad (3)$$

Since $T(x) \lesssim \|x\|_2^{-1}$, we have by the spherical integration factor of \mathbb{R}^3 that $|\int T(x) \varphi(x) dx| \leq C_\varphi < \infty$ for every $\varphi \in \mathcal{S}(\mathbb{R}^3)$. It follows that $T_\lambda(x) = T(x) e^{-\lambda \|x\|_2}$ can also be identified with a tempered distribution. Lemma 1 shows

$$\lim_{\lambda \rightarrow 0^+} \int \mathcal{F}\{T_\lambda\}(\omega) \varphi(\omega) d\omega = \int \mathcal{F}\{T\}(\omega) \varphi(\omega) d\omega$$

for all $\varphi \in \mathcal{S}(\mathbb{R}^3)$, given that $T \in \mathcal{S}'(\mathbb{R}^3) \cap L^1_{\text{loc}}(\mathbb{R}^3)$ is a tempered function of polynomial growth.

Upon confirmation that $\lim_{\lambda \rightarrow 0^+} \mathcal{F}\{T_\lambda\}$ is also a tempered function of polynomial growth, we will have that $(\varphi \lim_{\lambda \rightarrow 0^+} \mathcal{F}\{T_\lambda\})$ is absolutely integrable. The immediate consequence from Lebesgue dominated convergence theorem is

$$\int \mathcal{F}\{T\}(\omega) \varphi(\omega) d\omega = \int \left(\lim_{\lambda \rightarrow 0^+} \mathcal{F}\{T_\lambda\}(\omega) \right) \varphi(\omega) d\omega.$$

Since $T_\lambda \in L^1(\mathbb{R}^3)$, we may directly evaluate $\lim_{\lambda \rightarrow 0^+} \mathcal{F}\{T_\lambda\}$ while maintaining equality to $\mathcal{F}\{T\}$ and circumventing the need to rely on identity (3).

With this in mind, we suppress the limit notation of our left-hand side equalities and carry-on with the integration

$$\begin{aligned} \mathcal{F}\{T\}(\omega) &= \lim_{\lambda \rightarrow 0^+} 2u_y \frac{A}{\|a\|_2} \int_0^\infty \int_{-\pi/2}^{\pi/2} \int_{-\pi/2}^{\pi/2} (r \sin \theta \sin \phi) \\ &\quad (\sin(r\omega_x \sin \phi \cos \theta) \sin(r\omega_z \sin \theta) e^{-\lambda r}) d\phi d\theta dr. \end{aligned}$$

Apply trigonometric identity

$$\sin(x) \sin(y) = (\cos(x - y) - \cos(x + y))/2,$$

and integrate with respect r ,

$$\begin{aligned} \mathcal{F}\{T\}(\omega) &= \lim_{\lambda \rightarrow 0^+} -u_y \frac{A}{\|a\|_2} \int_{-\pi/2}^{\pi/2} \int_{-\pi/2}^{\pi/2} (\sin \theta \sin \phi) \cdot \\ &\quad \left(\frac{\lambda^2 - (\omega_x \sin \phi \cos \theta + \omega_z \sin \theta)^2}{(\lambda^2 + (\omega_x \sin \phi \cos \theta + \omega_z \sin \theta)^2)^2} - \frac{\lambda^2 - (\omega_x \sin \phi \cos \theta - \omega_z \sin \theta)^2}{(\lambda^2 + (\omega_x \sin \phi \cos \theta - \omega_z \sin \theta)^2)^2} \right) d\phi d\theta. \end{aligned}$$

As shown by corollary 1, this integrand can be proportionally dominated by the $\lambda = 0$ evaluation. By dominated convergence theorem

$$\begin{aligned} \mathcal{F}\{T\}(\omega) &= -4u_y \frac{A}{\|a\|_2} \int_{-\pi/2}^{\pi/2} \int_{-\pi/2}^{\pi/2} \\ &\quad \left(\frac{\omega_x \omega_z \sin^2 \theta \cos \theta \sin^2 \phi}{(\omega_x^2 \sin^2 \phi \cos^2 \theta - \omega_z^2 \sin^2 \theta)^2} \right) d\phi d\theta. \end{aligned}$$

Consider the change of variables $t = \sin \theta$ and integrate with respect to t using a partial fraction decomposition,

$$\begin{aligned} \mathcal{F}\{T\}(\omega) &= -8u_y \omega_z \frac{A}{\omega_x \|a\|_2} \int_0^{\pi/2} \left(\frac{1}{1 + (\omega_z^2/\omega_x^2) \csc^2 \phi} \right) \cdot \\ &\quad \left(\frac{1}{\omega_z^2} + \frac{1}{\omega_x^2} \frac{\csc^2 \phi \tanh^{-1}(1 + (\omega_z^2/\omega_x^2) \csc^2 \phi)^{-1/2}}{\sqrt{1 + (\omega_z^2/\omega_x^2) \csc^2 \phi}} \right) d\phi \end{aligned}$$

For brevity we will consider the shorthands

$$\mathcal{F}\{T\}(\omega) = -8u_y \omega_z \frac{A}{\omega_x \|a\|_2} \left(\frac{I_1}{\omega_z^2} + \frac{I_2}{\omega_x^2} \right).$$

Calculating first integration term I_1

$$\frac{I_1}{\omega_z^2} = \frac{1}{\omega_z^2} \int_0^{\pi/2} \frac{1}{1 + (\omega_z^2/\omega_x^2) \csc^2 \phi} d\phi = \frac{\pi}{2} \frac{1}{\omega_z^2} \left(1 - \frac{|\omega_z|}{\|\omega\|_2} \right).$$

This equality follows from $\lim_{x \rightarrow \pi/2} c \tan^{-1}(\tan(x)/c) = |c|$ and $\omega_x > 0$. Next with trigonometric identity

$$\csc^2(\phi) = 1 + \cot^2(\phi),$$

introduce change of variables $t = \cot(\phi)$ and shorthands $\rho^2 = 1 + (\omega_z^2/\omega_x^2)$ and $\kappa^2 = \rho^2 - 1$ to simplify the second integration term as

$$I_2 = \int_0^\infty \frac{1}{(\rho^2 + \kappa^2 t^2)^{3/2}} \tanh^{-1} \frac{1}{\sqrt{\rho^2 + \kappa^2 t^2}} dt$$

Calculating I_2

$$\begin{aligned} I_2 &= 0 + \frac{1}{\rho^2} \int_0^\infty \frac{t^2 dt}{(1 + t^2)(\rho^2 + \kappa^2 t^2)} \\ &= \frac{\pi}{2} \left(\frac{1}{\rho|\kappa|} - \frac{1}{\rho^2} \right). \end{aligned}$$

Here a partial fraction decomposition was used on the integration-by-parts integral. Written in terms of ω ,

$$\frac{I_2}{\omega_x^2} = \frac{\pi}{2} \frac{1}{\omega_z^2} \left(\frac{|\omega_z|}{\|\omega\|_2} - \frac{\omega_z^2}{\|\omega\|_2^2} \right).$$

Summed together with equality $\omega_x^2 = \|\omega\|_2^2 - \omega_z^2$,

$$\mathcal{F}\{T\}(\omega) = -4\pi u_y \frac{A}{\|a\|_2} \frac{\omega_x}{\omega_z} \frac{1}{\|\omega\|_2^2}.$$

Lastly expanding A in terms of the original, canonical coordinates

$$\mathcal{F}\{T\}(\omega) = \frac{4\pi i(u \cdot \widehat{\omega} \times a)}{\|\omega\|_2} e^{i\omega \cdot \frac{u_1 + \hat{p}_0}{2}} \frac{\text{sinc}\left(\frac{\omega \cdot a}{2}\right)}{\sqrt{1 - (\hat{\omega} \cdot \hat{a})^2}}. \quad (4)$$

Note that as

$$\left| \lim_{\lambda \rightarrow 0^+} \mathcal{F}\{T_\lambda\}(\omega) \right| \lesssim \|\omega\|_2^{-1}$$

we confirm our earlier claim that the pointwise limit of $\mathcal{F}\{T_\lambda\}$ is a tempered function of polynomial growth in \mathbb{R}^3 .

When combined with the v measurement contribution, we obtain the final closed-form solution to the sinusoidal sensitivity model. Examples of simulated sensitivities and bias fields for different grids G can be found in Appendix B.

4 | SAMPLING WITH THE SINUSOIDAL SENSITIVITY MODEL

Consider the sparse Fourier sampler

$$J(\eta) = \sum_{\omega \in G} \delta(\eta - \omega)$$

where $\delta(\cdot - \omega)$ is the Dirac delta distribution centered at ω . Understood formally, the sinusoidal sensitivity model can be expressed in terms of this sampler as

$$S(x) = \mathcal{F}^{-1}\{J \mathcal{F}\{\bar{B}\}\}(x).$$

The issue in this sampler is that it is only well-defined for functions f which have meaningful point evaluations. The framework used in section 3 worked with class $\mathcal{F}\{\bar{B}\} \in L_{\text{loc}}^1(\mathbb{R}^3)$ whose behavior is only specified with respect to an integrating action against the Lebesgue measure on \mathbb{R}^3 .

In hopes to extend the sinusoidal model to work better with the equivalence class $\mathcal{F}\{\bar{B}\}$ we may consider the generalized sampler

$$J_R = \sum_{\omega \in G} \frac{1}{\text{vol}(B(\omega, R))} \chi_R(\eta; \omega)$$

where $\chi_R(\eta; \omega) = 1\{\|\eta - \omega\|_2 < R\}$ is the R -cutoff function centered at ω and $\text{vol}(B(\omega, R))$ is the volume of the R -radius sphere centered at ω . We see then for $R > 0$, the generalized sinusoidal model

$$S_R(x) = \mathcal{F}^{-1}\{J_R \mathcal{F}\{\bar{B}\}\}(x)$$

does produce a well-defined result.

Ideally we would like limit $\lim_{R \rightarrow 0^+} S_R$ to be equivalent to our original sinusoidal sensitivity model. Before continuing, we introduce the following term for notational clarity. With $q = u + iv$ consider

$$g(\omega) = \frac{4\pi i(q \cdot \widehat{\omega \times a})}{\|\omega\|_2} \text{sinc}\left(\frac{\omega \cdot a}{2}\right) \sqrt{1 - (\hat{\omega} \cdot \hat{a})^2} \frac{e^{i\omega \cdot \frac{p_1 + p_0}{2}}}{e^{i\omega \cdot x}}$$

which lies in the space of continuous functions. That is have $g(\omega) \in C(\mathbb{R}^3 \setminus \{0\})$ and $e^{-i\omega \cdot x} \mathcal{F}\{\bar{B}\}(\omega) \in L^1_{\text{loc}}(\mathbb{R}^3)$. One can show that these objects satisfy the limit equality

$$g(\omega) = \lim_{R \rightarrow 0^+} \frac{1}{\text{vol}(B(\omega, R))} \int_{\|\eta - \omega\|_2 < R} e^{-i\eta \cdot x} \mathcal{F}\{\bar{B}\}(\eta) d\eta.$$

To see this, note that for continuity point ω we have

$$|e^{-i\eta \cdot x} \mathcal{F}\{\bar{B}\}(\eta) - g(\omega)| < \varepsilon$$

for almost every η less than a suitable radius R from ω . With shorthand $\langle f, g \rangle_\eta = \int f(\eta) g(\eta) d\eta$ and ω -centered indicator $\chi_R(\eta; \omega) = 1\{\|\eta - \omega\|_2 < R\}$, it follows that

$$\begin{aligned} \left| \langle e^{-i\eta \cdot x} \mathcal{F}\{\bar{B}\}, \chi_R \rangle_\eta - g(\omega) \right| &\leq \langle |e^{-i\eta \cdot x} \mathcal{F}\{\bar{B}\} - g(\omega)|, \chi_R \rangle_\eta \\ &< \langle \varepsilon, \chi_R \rangle_\eta \\ &= \text{vol}(B(\omega, R)) \cdot \varepsilon. \end{aligned}$$

As a consequence the equality

$$S(x) = \lim_{R \rightarrow 0^+} S_R(x) \quad \text{for all } x \in \mathbb{R}^3,$$

is well-defined with $S = \mathcal{F}^{-1}\{Jg\}$ and any grid sampler J which does not contain the origin.

5 | IMPLEMENTATION

A CUDA accelerated implementation `biasgen` can be found on GitHub*. This Python package takes in user-defined RF coil positions and sampling information to produce custom 3-dimensional bias fields. A coil positioning and visualization tool is provided for setup as well as various examples to help the user get started. As the bias generation is done independently from image intensity, `biasgen` can be used both to produce simulated dataset and augment existing ones. An application of `biasgen` on the BrainWeb phantom dataset can be found in Appendix B.

6 | CONCLUSIONS

In this paper, we have derived the Fourier transform of measured magnetic field emitted by line segment geometries. This closed-form can be used to evaluate the sinusoidal sensitivity model to arbitrary accuracy and function smoothness. Special care was taken to discuss the distributional nature of the solved Fourier transform and settings were identified where this closed-form agreed with the sparse sampled model introduced by Ref. [6]. As next steps, further work can be done to solve (1) for smooth line curves, such as for the case of circular or cylindrical geometries.

ACKNOWLEDGMENTS

Research reported in this manuscript was partially supported by the NIBIB of the National Institutes of Health under award number R21EB026086. The content is solely the responsibility of the authors and does not necessarily represent the official views of the National Institutes of Health.

Conflict of interest

The authors declare no potential conflict of interests.

REFERENCES

1. Deshmane A, Gulani V, Griswold MA, Seiberlich N. Parallel MR imaging. *Journal of magnetic resonance imaging : JMRI*. 2012;36(1):55-72.
2. Tustison NJ, Avants BB, Cook PA, et al. N4ITK: Improved N3 Bias Correction. *IEEE Transactions on Medical Imaging*. 2010;29(6):1310-1320.
3. Wells WM, Grimson WEL, Kikinis R, Jolesz FA. Adaptive segmentation of MRI data. *IEEE Transactions on Medical Imaging*. 1996;15(4):429-442.
4. Simko AT, Löfstedt T, Garpebring A, Nyholm T, Jonsson J. MRI bias field correction with an implicitly trained CNN. In: ; 2022.
5. Cocosco CA, Kollokian V, Kwan RKS, Evans AC. BrainWeb: Online Interface to a 3D MRI Simulated Brain Database. *NeuroImage*. 1997;5(4).
6. Guerquin-Kern M, Lejeune L, Pruessmann KP, Unser M. Realistic Analytical Phantoms for Parallel Magnetic Resonance Imaging. *IEEE Transactions on Medical Imaging*. 2012;31(3):626-636.
7. Uecker M, Ong F, Tamir JI, et al. Berkeley advanced reconstruction toolbox. *Proc. Intl. Soc. Mag. Reson. Med.* 2015;23(2486).

*<https://github.com/lucianoAvinas/biasgen>

How to cite this article: Vinas L, and Sudyadhom A (2022), Sinusoidal Sensitivity Calculation for Segment Geometries, *Magn Reson Med.*, .

APPENDIX

A AUXILIARY LEMMAS

A.1 A Specific Tempered Function Convergence

Definition 1 (Polynomial Growth Tempered Functions). We say locally integrable $T \in L^1_{\text{loc}}(\mathbb{R}^n)$ has polynomial growth $m > 0$ if there exists some constant C such that for all $R \geq 1$,

$$\int_{\|x\|_2 \leq R} |T(x)| dx \leq CR^m.$$

As the action $\langle T, g \rangle = \int T(x)g(x) dx$ with any locally integrable T defines a tempered distribution for $g \in \mathcal{S}(\mathbb{R}^n)$, we will sometimes make the distinction between the tempered function T and the tempered distribution T . A consequence of definition 1, is that for every polynomial-growing tempered function T there is some R' such that $T(x)$ is dominated as

$$|T(x)| \leq C' \|x\|_2^{m-n-2},$$

for $\|x\| \geq R'$ and some constant $C' > 0$.

Lemma 1. Let T be a tempered function of polynomial growth $m_0 > 0$ and define $T_\lambda(x) = T(x)e^{-\lambda\|x\|_2}$. Then for every $\varphi \in \mathcal{S}(\mathbb{R}^n)$ we have

$$\lim_{\lambda \rightarrow 0^+} \int \mathcal{F}\{T_\lambda\}(\omega) \varphi(\omega) d\omega = \int \mathcal{F}\{T\}(\omega) \varphi(\omega) d\omega.$$

Proof. Note by identity (3) and the fact $\mathcal{F} : \mathcal{S}(\mathbb{R}^n) \rightarrow \mathcal{S}(\mathbb{R}^n)$ is bijective, it suffices to show

$$\lim_{\lambda \rightarrow 0^+} \int T_\lambda(x) \varphi(x) dx = \int T(x) \varphi(x) dx \quad \forall \varphi \in \mathcal{S}(\mathbb{R}^n).$$

Introduce shorthands $\chi_R(x) = 1_{\{\|x\|_2 \leq R\}}$ and $\langle \phi, \varphi \rangle = \int \phi(x) \varphi(x) dx$ for every $(\phi, \varphi) \in \mathcal{S}'(\mathbb{R}^n) \times \mathcal{S}(\mathbb{R}^n)$. It follows that

$$\begin{aligned} |\langle T_\lambda, \varphi \rangle - \langle T, \varphi \rangle| &\leq |\langle T\chi_R - T, \varphi \rangle| + |\langle T_\lambda\chi_R - T\chi_R, \varphi \rangle| + \\ &\quad |\langle T_\lambda - T_\lambda\chi_R, \varphi \rangle| \\ &\leq 2|\langle T\chi_R - T, \varphi \rangle| + |\langle T_\lambda\chi_R - T\chi_R, \varphi \rangle|. \end{aligned}$$

Given the rapid-decay of Schwartz functions $\varphi \in \mathcal{S}(\mathbb{R}^n)$ there exists sufficiently large R'' such that

$$\left| \int_{\|x\|_2 > R} T(x) \varphi(x) dx \right| \leq \left| \int_{\|x\|_2 > R} T(x) \|x\|^{-m_0} dx \right|,$$

for $R \geq R''$. The growth conditions on T imply that this upperbound goes to 0 as $R \rightarrow \infty$. That is, for every $\varepsilon > 0$

there is some R_0 such that

$$R \geq R_0 \Rightarrow |\langle T\chi_R, \varphi \rangle - \langle T, \varphi \rangle| < \varepsilon/4.$$

Furthermore note that this relationship is monotonic such that a decrease in ε produces a non-strict increase in R_0 . Using the integrability of $T\chi_R \in L^1(\mathbb{R}^n)$

$$\begin{aligned} |\langle T_\lambda\chi_R, \varphi \rangle - \langle T\chi_R, \varphi \rangle| &\leq \|T\chi_R\varphi\|_{L^1} \left\| \chi_R (1 - e^{\lambda\|x\|_2}) \right\|_{L^\infty} \\ &\leq (1 - e^{-\lambda R}) \sup_{x \in \mathbb{R}^n} |\varphi(x)| \|T\chi_R\|_{L^1} \\ &\leq (1 - e^{-\lambda R}) c_\varphi C_R \end{aligned}$$

where $c_\varphi, C_R < \infty$ by assumption on φ and $T\chi_R$. Collect both constants into one constant C_{φ, R_0} . If $C_{\varphi, R_0} \leq \varepsilon/2$ then directly plugging in gives

$$|\langle T_\lambda, \varphi \rangle - \langle T, \varphi \rangle| < \varepsilon \quad \text{for all } \lambda > 0.$$

For the complementary condition $C_{\varphi, R_0} > \varepsilon/2$ we have

$$\lambda < -\log(1 - \varepsilon/(2C_{\varphi, R_0}))/R_0 \Rightarrow |\langle T_\lambda, \varphi \rangle - \langle T, \varphi \rangle| < \varepsilon.$$

As this can be done for any $\varphi \in \mathcal{S}(\mathbb{R}^n)$, we arrive at the desired relation

$$\lim_{\lambda \rightarrow 0^+} \int \mathcal{F}\{T_\lambda\}(\omega) \varphi(\omega) d\omega = \int \mathcal{F}\{T\}(\omega) \varphi(\omega) d\omega. \quad \square$$

A.2 Domination of a Specific Rational Function

Lemma 2. For any $a, b \in \mathbb{R}$ we have

$$\left| \frac{\lambda^2 - (a+b)^2}{(\lambda^2 + (a+b)^2)^2} - \frac{\lambda^2 - (a-b)^2}{(\lambda^2 + (a-b)^2)^2} \right| \lesssim \frac{1}{(a-b)^2} - \frac{1}{(a+b)^2}$$

for all $\lambda \in \mathbb{R}$.

Proof. Let A be a placeholder value for the absolute value term in the lemma description. With some manipulations

$$\begin{aligned} A &= 4|ab| \left| \frac{3\lambda^4 + 2\lambda^2(a^2 + b^2) - (a^2 - b^2)^2}{(\lambda^2 + (a+b)^2)^2(\lambda^2 + (a-b)^2)^2} \right| \\ &\leq 4|ab| \left| \frac{3\lambda^4 + 6\lambda^2(a^2 + b^2) + 3(a^2 - b^2)^2}{(\lambda^2 + (a+b)^2)^2(\lambda^2 + (a-b)^2)^2} \right| \\ &= 3 \left| \frac{4ab}{(\lambda^2 + (a+b)^2)(\lambda^2 + (a-b)^2)} \right| \\ &\leq 3 \left| \frac{4ab}{(a^2 - b^2)^2} \right| \\ &= 3 \operatorname{sgn}(ab) \left(\frac{1}{(a-b)^2} - \frac{1}{(a+b)^2} \right) \end{aligned} \quad \square$$

Define a λ -parameterized function $f : D \rightarrow \mathbb{R}$ where

$$f(\eta; \lambda) = c \left(\frac{\lambda^2 - (a+b)^2}{(\lambda^2 + (a+b)^2)^2} - \frac{\lambda^2 - (a-b)^2}{(\lambda^2 + (a-b)^2)^2} \right)$$

and a, b, c are all functions of η .

Corollary 1. Suppose functions a, b, c satisfy

$$\text{sgn}(a(\eta)b(\eta)c(\eta)) = \text{sgn}(a(\eta')b(\eta')c(\eta'))$$

for all $\eta, \eta' \in D$. Then for integrable $f(\eta; 0)$ we have

$$\lim_{\lambda \rightarrow 0^+} \int f(\eta; \lambda) d\eta = \int f(\eta; 0) d\eta.$$

Proof. Note a simple extension of Lemma 2 shows

$$\left| c \left(\frac{\lambda^2 - (a+b)^2}{(\lambda^2 + (a+b)^2)^2} - \frac{\lambda^2 - (a-b)^2}{(\lambda^2 + (a-b)^2)^2} \right) \right| \leq 3c \text{sgn}(abc) \cdot \left(\frac{1}{(a-b)^2} - \frac{1}{(a+b)^2} \right).$$

As $\text{sgn}(abc)$ is fixed for every $\eta \in D$, we have that $3 \text{sgn}(abc) f(\eta; 0)$ dominates $|f(\eta; \lambda)|$ for all $\lambda \in \mathbb{R}_{>0}$. \square

B SIMULATED BIAS FIELDS

The following examples are a series of bias field simulations which take sensitivity equation

$$S(x) = \sum_{\omega \in G} e^{-i\omega \cdot x} \mathcal{F}\{\bar{B}(x)\}(\omega)$$

a combine the resulting sensitivity maps $S_k(r)$ using sum-of-squares approach to produce bias field

$$\bar{S}(r) = \left(\sum_{k=1}^N S_k^2(r) \right)^{1/2}.$$

Grid G is a collection of $(2L)^3 - 1$ points in $\mathbb{R}^3 \setminus \{0\}$ parameterized by a half-width L , a spacing factor $s = (s_x, s_y, s_z)$, and a starting shift $c = (c_x, c_y, c_z)$. All bias fields are superimposed on central T1 slices of the BrainWeb dataset through an element-wise product application.

B.1 Smooth Three Coil Bias

Bias fields were generated by three rectangular coils and grid settings $L = 7, s = (1.5, 1.5, 1.5), c = (0, 0, 0)$.

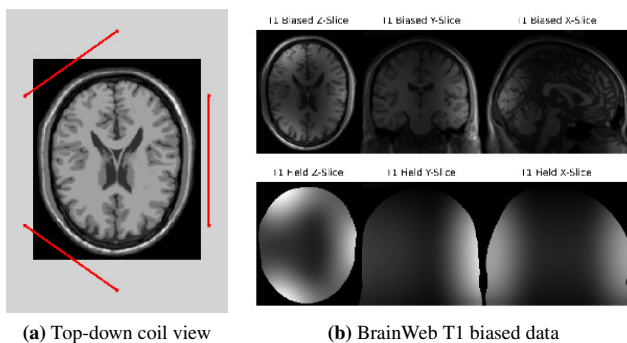


FIGURE B1 Smooth bias field visualization with top-down view of the coil geometry for reference.

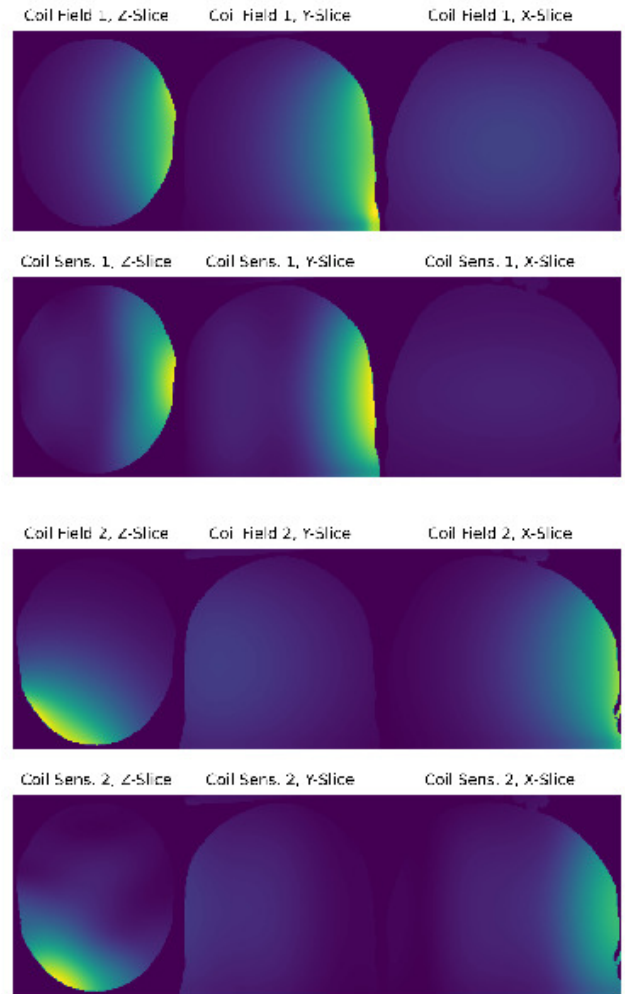


FIGURE B2 Emitted field and sensitivity comparison for coil subset.

B.2 Rough Three Coil Bias

Bias fields were generated by three rectangular coils and grid settings $L = 12, s = (1.75, 1.75, 0.5), c = (-0.25, -0.25, 0)$.

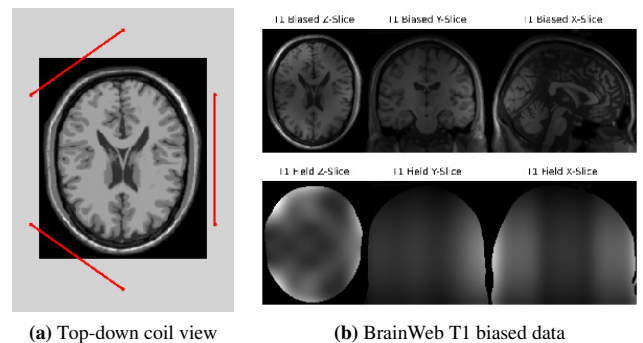


FIGURE B3 Rough bias field visualization with top-down view of the coil geometry for reference.

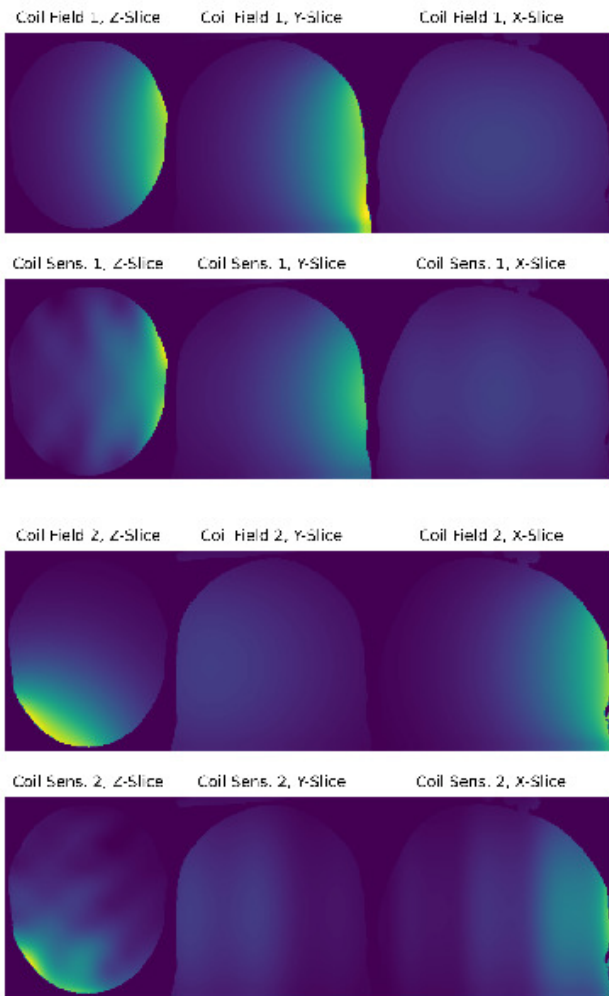


FIGURE B4 Emitted field and sensitivity comparison for coil subset.